Modeling and stochastic analysis of the single photon response

Jürgen Reingruber, David Holcman

Abstract

Rod photoreceptors have the remarkable ability to respond to a single photon. A photon absorption triggers the activation of a receptor which is subsequently amplified by the activation of only 5-10 molecules. Because of such low numbers, the activation process has to be proceed in a coordinated manner in order to generate a reproducible signal. In addition, this signal has to overcome the background noise generated by spontaneous activations and deactivation of millions of enzymatic molecules. We review here recent modeling and stochastic analysis of the molecular events underlying the single photon response and the background noise. The homogenization procedure of the rod geometry is the first step for reducing the three into one dimensional, so that numerical simulations become possible and reveal the fundamental relation between proteins concentrations, biochemical rate constanct and rod geometry. The stochastic modeling is used to analyse electrophysiological recordings and to extract in vivo biochemical constants. Modeling phototransduction has evolved at the far front of cell transduction and system and thus the approach presented here can be apply to any transduction mechanisms.

1 Introduction

Signal transduction at a single molecular level is based on stochastic biochemical events occurring in constrained cellular microdomains. Molecular fluctuations in the transduction pathway generate a cellular background noise, which sets the limit of cell detection. This limit is generic to most of transduction mechanisms that consists of converting a molecular signal into a cellular response. For photoreceptors, light (photons) is transformed into a cellular change of the voltage potential called a hyperpolarization (decrease of the voltage) due to the exit of ions, For olfactory cells, a single odorant molecule can activate a flow of ions through voltage gated channels. During synaptic transmission, neurotransmitters generate a local depolarization. Finally, a transcription factor in the cell nucleus activates or regulate genes, leading to protein expression. In all of this example a molecular signal lead to a cellular response, but how such a signal overcome the noise and what is the nature of the molecular and cellular noise. We will explore this question based on modeling and analysis of the single photon response in photoreceptors.

A key step in the cellular response to a small molecular event is the amplification of the signal, which occurs by a protein (G-protein)cascades. Of all the G-protein cascades in nature, the best-understood are those initiated by the absorption of a photon in *Drosophila* microvilli [1, 2] and in the outer segment (OS) of vertebrate rod photoreceptors (Fig. 1) [1, 3, 4]. The rods of amphibians and mammals have been shown to have the remarkable ability to detect single-photons of light above background noise [5, 6]. But amphibian and mammalian rods differ in concentrations and biochemical properties of proteins involved in the light response, and by as much as an order of magnitude in the diameter of their disk membranes, where the reactions of the cascade take place. It remains largely unknown how the biochemistry and the geometry adapt to guarantee a reliable macroscopic response initiated by a single molecular event.

We summarize in this review recent progress in mathematical modeling of single photon response in rod photoreceptors. The modeling, analysis and simulations combines several methods. First, because it is yet not possible to model millions of interacting molecules, the three dimensional geometry of the rod geometry is reduced to a one dimension. This is possible because diffusion in a thin cylinder is well approximated by a one dimension process. In that context, reaction-diffusion equations can be written for the subcellular molecular interactions occurring inside the rod structure. Second, there a geometrical separation between chemical reactions occurring on the membrane and others inside the three dimensional cytoplasm. This geometrical separation allows studying separately two- an three- dimensional chemical reactions. Two dimensional chemical-reactions do not rely on suffer from geometrical confinement and studied using a Markov chains. However, connecting the output of two-dimensional reactions with the three dimensional ones uses the one-dimensional diffusion reduction approximation. The overall reduced modeling allows to perform stochastic simulations that explain the variability in the biochemistry and allow to study the major source of noise during a single-photon response.

We recall briefly that noise in the photoreceptor is generated by the fluctuations in the activity of a critical enzyme called phosphodiesterase (PDE). This enzyme fulfills two essential functions. First, the phosphodiesterase that becomes activated through the transduction cascade after a photon absorption (light-activated PDE) increases the hydrolysis of cGMP, a diffusible second messenger controlling the opening of ionic membrane channels, leading to channel closure and cell hyperpolarization; second, spontaneously activated PDE is necessary to maintain in darkness a steady-state cGMP concentration and to set the cGMP turnover rate, an important determinant of the time scale of the photon response [7, 8] (Fig. 2). Fluctuations in the number of spontaneously activated PDEs generate a background noise that is commonly referred to as the dark noise [9, 7, 10]. The main source of variability in the amplitude of the single-photon response is due to variability in the number of light-activated PDEs [11, 12, 6, 13].

Photon response curve and noise generated within the transduction cascade are evaluated using spatially resolved reaction-diffusion equations and stochastic simulations of PDE activations at the level of single molecules. We present here a summary of multiscale simulations that account for the molecular details (PDE activations and cGMP hydrolysis) and the intrinsic molecular noise called dark noise. The result of the simulations can be directly compared to experimental recordings and the analytical expressions for the dark noise power spectrum are used to extract the values of key parameters from the analysis of measured current recorded in Wild type (WT) and but also in genetically modified cells such as $\text{Caps}^{-/-}$ knockout mice.

This review is organized as follows: in the first part, we present the homogenization procedure to reduce the three-dimensional rod outer-segment geometry to a one dimensional with an effective diffusion coefficient. In the second part, Markov chains are used for modeling the stochastic activation of PDE molecules following a photon absorption. We also present the modeling of the spontaneous PDE activation. In the third, we analyze the Laplace equation to computing the cGMP hydrolysis rate, based on the narrow escape theory in narrow band [14]. In section four, we introduce the coupled system of equations for cGMP and calcium currents. In section five, we present the stochastic simulations of a single photon response. Finally, in the last section, we explain how numerical simulations are used to extract biophysical parameters from dark noise recordings and single photon response.

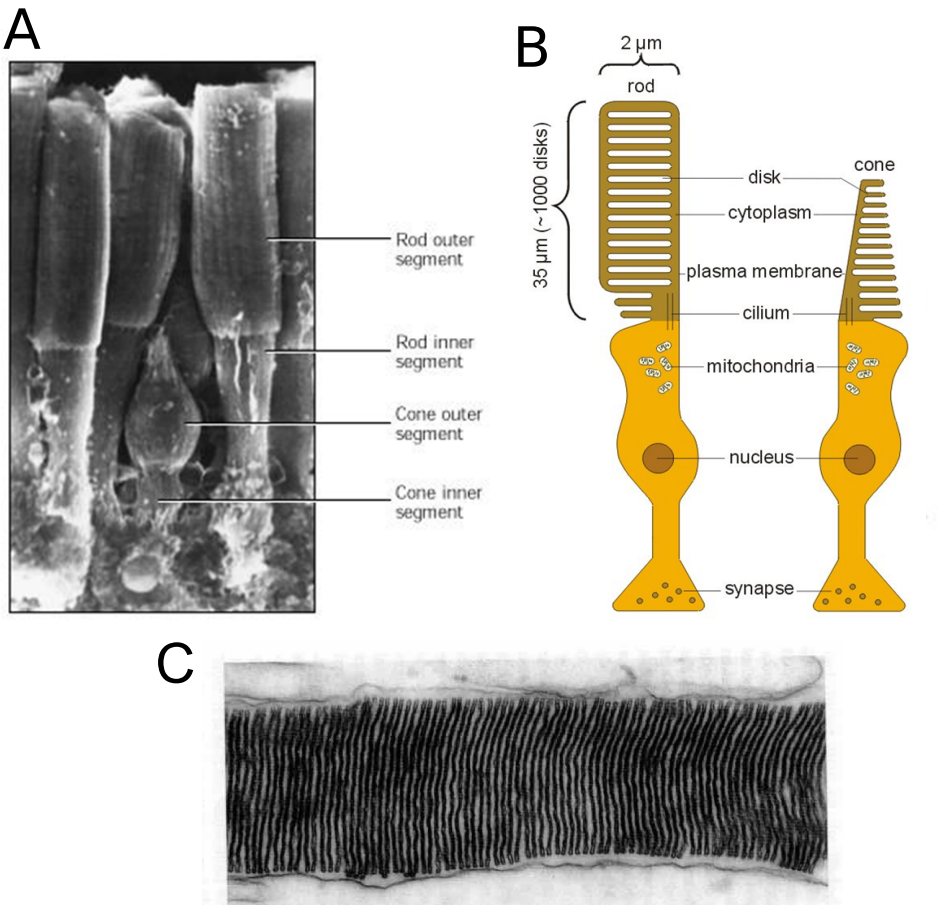

Fig. 1: **Geometrical organization of rod and cone photoreceptors.** (A)Electron Microcopy (EM) image of rods and cones located in the retina. (B) Schematic modeling of a rod and a cone showing their polarized structure: light sensitive outer segment, inner segment with nucleus and synaptic terminal.(C) Cross section of a rod outer segment: internal disks divide the outer segment into almost independent cylindrical compartments.

2 Modeling phosphodiesterase (PDE) activation after a photon absorption using Markov chain

To simulate the time course of the stochastic number of activated PDE P^* following a single photon absorption, we use Markov chain [15] (see also [16]): after photon absorption, a rhodopsin molecule undergoes a conformational modification and changes from an inactive R into an active R_N^* state, where N is the total number of available phosphorylation sites. The R_N^* phosphorylation are catalyzed by a rhodopsin kinase (RK) that gradually reduces the activity of rhodopsin (Fig. 2A-B). Through phosphorylation, rhodopsin in the state R_n^* undergoes a transition to state R_{n-1}^*, modelled by the state dependent Poissonian phosphorylation rate λ_n. R_n^* activates the G-protein transducin T^* with rate k_n, which constitutes an amplification process. A T^* transducin binds to a single PDE with a rate μ_t and forms a complex denoted by P^* (see Fig 2A-C), which subsequently deactivates with rate μ_p. Eventually, the rhodopsin R_n^* becomes deactivated through another molecule arrestin binding with a rate μ_n. The kinetic reactions are summarized as follows (see table 1)

$$\begin{aligned} R_n^* &\xrightarrow{\lambda_n} R_{n-1}^* \\ R_n^* &\xrightarrow{\mu_n} R \\ R_n^* + T &\xrightarrow{k_n} R_n^* + T^* \\ T^* + P &\xrightarrow{\mu_t} P^* \\ P^* &\xrightarrow{\mu_p} P \end{aligned} \tag{1}$$

The state of the signalling process is described by three stochastic variables integer values (n, l, k),

Table 1: Parameters for PDE activation

Parameter	**Definition**
$\bar{P}^*_{sp,comp}$	Mean number of spontaneous actived PDE molecules per compartment
$\bar{P}^*_{li,max}$	Mean of the peak number of light-activated PDE
ρ_{pde}	PDE surface density
ν_{sp}	Spontaneous PDE activation rate
μ_{sp}	Spontaneous PDE deactivation rate
μ_{li}	Deactivation rate for light-activated PDE
τ_{rh}	Activated Rhodopsin lifetime
N_p	Number of Rhodopsin phosphorylation steps
$\gamma_{rt,max}$	Maximal transducin activation rate
ω	Decay rate of transducin activation with the number of phosphorylation steps
γ_{tp}	Rate by which activated transducin activates PDE

which are the phosphorylation state $0 \leq n \leq N$ of R^* (n corresponds to the number of remaining unphosphorylated sites), the number $0 \leq l \leq \infty$ of $T*$ and $0 \leq k \leq \infty$ for $P*$. The joint probability $P_n(l, k, t)$ satisfies the Master equation

$$\begin{aligned} \frac{\partial}{\partial t} P_n(l,k,t) &= \lambda_{n+1} P_{n+1}(l,k,t) + k_n P_n(l-1,k,t) \\ &\quad + \mu_t (l+1) P_n(l+1,k-1,t) + \mu_p (k+1) P_n(l,k+1,t) \\ &\quad - \left(\lambda_n + \mu_n + k_n + \mu_t l + \mu_p k\right) P_n(l,k,t). \end{aligned} \tag{2}$$

In state $n = 0$, all sites are phosphorylated and $\lambda_0 = 0$. After a photon absorption, R^* is in state $n = N$ and the number of T^* and P^* are zero. The initial condition is given by $P_n(l, k, 0) = \delta_{n,N}\delta_{l,0}\delta_{k,0}$, where ($\delta_{i,j}$ is the Kronecker symbol).

2.1 First and second moment (Mean and variance) of rhodopsin lifetime distribution

The mean and variance of R^* lifetime can be computed from the probabilities $P_n(t)$ to find $R*$ in state n at time t. By summing Eq. 2 over l and k, the probability vector $\vec{P}(t) = (P_N(t), \ldots, P_0(t))^\top$ satisfies the equation

$$\frac{d}{dt}\vec{P}(t) = \mathbf{S}\,\vec{P}(t) \quad \text{with} \quad \mathbf{S} = \begin{pmatrix} -\beta_N & & & \\ \lambda_N & -\beta_{N-1} & & \\ & & \vdots & \\ & & \lambda_1 & -\beta_0 \end{pmatrix} \tag{3}$$

and $\beta_n = \lambda_n + \mu_n$. To compute the mean R^* lifetime, we integrate Eq. 3 using the initial condition $\vec{P}(0) = (1, \ldots, 0)^\top$ and we use that $\vec{P}(t)$ vanishes for $t \to \infty$. We obtain for the mean time

$$\bar{\tau} = \sum_{n=0}^{N} \int_0^\infty P_n(t)dt = -\mathrm{Tr}\left(\mathbf{S}^{-1}\vec{P}(0)\right) = \sum_{n=0}^{N} \frac{1}{\beta_n} \prod_{k=n+1}^{N} p_k\,, \tag{4}$$

with $p_n = \frac{\lambda_n}{\beta_n}$. Eq. 4 has an intuitive interpretation: it is the sum of mean lifetimes $\frac{1}{\beta_n}$ in each state n multiplied by the probability to reach this state before being deactivated via arrestin binding (see also fig. 2E).

The variance is computed by integration by parts in the relation

$$\begin{aligned} \Sigma_\tau &= -\sum_{n=0}^{N} \int_0^\infty t^2 \frac{d}{dt} P_n(t)dt - \bar{\tau}^2 = \sum_{n=0}^{N} \int_0^\infty 2tP_n(t)dt - \bar{\tau}^2 = 2\mathrm{Tr}\left(\mathbf{S}^{-2}\vec{P}(0)\right) - \bar{\tau}^2 \\ &= 2\sum_{n=0}^{N}\sum_{j=0}^{n} \frac{1}{\beta_n}\frac{1}{\beta_j} \prod_{k=j+1}^{N} p_k - \bar{\tau}^2\,. \end{aligned} \tag{5}$$

The coefficient of variation (CV) of $R*$ lifetime (Fano factor) has a lower bound that depends only on the number of phosphorylation sites N [15]. Indeed using Eq. 4 and Eq. 5, we have

$$CV_\tau = \frac{\sqrt{\Sigma_\tau}}{\bar{\tau}} \geq \frac{1}{\sqrt{N}}\,. \tag{6}$$

The minimum $CV_\tau = \frac{1}{\sqrt{N}}$ is achieved for $\beta_n = const$ and $p_n = 1$. The first condition reduces the lifetime variability of the various deactivation states. The latter condition requires that arrestin binds only when R^* is fully phosphorylated, which maximizes the effective number of deactivation steps.

2.2 Stochastic analysis of the number of activated PDE

As shown in the previous paragraph, multiple phosphorylations of the rhodospin molecule reduces the CV_τ and lead to a more reliable R^* deactivation process. Is a reliable R^* deactivation process leads to a minimal variance in the number of P^*? how multiple phosphorylations affect the mean

and variance of the number of activated PDE? In particular, does a low CV_τ entail a low CV of the number of activated PDE? The answer to these questions is based on a system of differential equations to compute numerically the time dependent mean and variance of P^* and the mean and variance of the total number of P^* that are activated during a single photon response. We now present such equations.

2.2.1 System of differential equations for mean and variance

The mean and variance that depend only on the phosphorylation state n of R^* can be computed by decomposing the matrix $\mathbf{S}$ into a sum of left eigenvectors. By decomposing the activation rate vector $\vec{k} = (k_N, \ldots, k_0)^\top$ into N eigenvectors $\vec{k}_i$ of the matrix $\mathbf{S}$, we get

$$\vec{k} = \sum_{i=0}^{N} \vec{k}_i \quad \text{with} \quad \vec{k}_i^\top \mathbf{S} = -\beta_i \vec{k}_i^\top \,, \tag{7}$$

we obtain for the individual mean values the relation

$$\frac{d}{dt}\bar{k}_i(t) = \frac{d}{dt}\sum_{n=0}^{N} k_{i,n} P_n(t) = \sum_{n,m=0}^{N} k_{i,n}\mathbf{S}_{n,m} P_m(t) = -\beta_i \bar{k}_i(t)\,. \tag{8}$$

Together with the initial condition $\vec{P}(0) = (1, \ldots, 0)^\top$, we get

$$\bar{k}(t) = \sum_{i=0}^{N} \bar{k}_i(t) = \sum_{i=0}^{N} k_{i,N}\, e^{-\beta_i t}\,. \tag{9}$$

Similarly, the variance $\Sigma_k(t) = \sum_{n=0}^{N} k_n^2 P_n(t) - \bar{k}(t)^2$ is calculated by decomposing the vector $\vec{x} = (k_N^2, \ldots, k_0^2)$.

We now present the time dependent mean and variance of PDE defined by

$$\bar{P}(t) = \sum_{n=0}^{N}\sum_{l,k=0}^{\infty} k P_n(l,k,t) \quad \text{and} \quad \Sigma_p(t) = \sum_{n=0}^{N}\sum_{l,k=0}^{\infty} k^2 P_n(l,k,t) - \bar{P}(t)^2. \tag{10}$$

Using Eq. 2, it is possible to obtain a closed system of differential equations for the mean and cross-correlations,

$$\begin{aligned}
\frac{d}{dt}\bar{T}(t) &= -\mu_t \bar{T}(t) + \bar{k}(t) \\
\frac{d}{dt}\bar{P}(t) &= -\mu_p \bar{P}(t) + \mu_t \bar{T}(t) \\
\frac{d}{dt}\Sigma_t(t) &= -2\mu_t \Sigma_t(t) + \mu_t \bar{T}(t) + 2\Sigma_{kt}(t) + \bar{k}(t) \\
\frac{d}{dt}\Sigma_p(t) &= -2\mu_p \Sigma_p(t) + 2\mu_t \Sigma_{tp}(t) + \mu_t \bar{T}(t) + \mu_p \bar{P}(t) \\
\frac{d}{dt}\Sigma_{tp}(t) &= -(\mu_t + \mu_p)\Sigma_{tp}(t) + \mu_t \Sigma_t(t) - \mu_t \bar{T}(t) + \Sigma_{kp}(t)\,.
\end{aligned} \tag{11}$$

The mean activation rate $\bar{k}(t)$ can be computed independently and therefore is an input function.

To close this system we need additional equations for $\Sigma_{kp}(t)$ and $\Sigma_{kt}(t)$. Using the decomposition in Eq. 7, we write

$$\Sigma_{kt}(t) = \sum_i \Sigma_{k_i t}(t) \quad \text{and} \quad \Sigma_{kp}(t) = \sum_i \Sigma_{k_i p}(t)\,. \tag{12}$$

Finally, the missing equations that close the system are

$$\begin{aligned}\frac{d}{dt}\Sigma_{k_i t}(t) &= -(\beta_i+\mu_t)\Sigma_{k_i t}(t)+\sum_j \Sigma_{k_i k_j}(t)\\ \frac{d}{dt}\Sigma_{k_i p}(t) &= -(\beta_i+\mu_p)\Sigma^2_{k_i p}(t)+\mu_t\Sigma_{k_i t}(t)\,.\end{aligned} \tag{13}$$

The correlation functions $\Sigma_{k_i k_j}(t)=\sum_n k_{i,n}k_{j,n}P_n(t)-\bar{k}_i(t)\bar{k}_j(t)$ and $\bar{k}(t)$ are known functions.

2.3 Stochastic dynamics of the number of activated PDE

To further investigate how the variability of $R*$ deactivation can influence the production of P^*, it is useful to compute the mean $\bar{P}_{tot}$ and variance $\Sigma_{p_{tot}}$ of the total number of P^* produced during a SPR. This computation is obtained by setting the P^* deactivation rate to zero, $\mu_p=0$, in which case all P^* are conserved. We obtain

$$\bar{P}_{tot} = \int_0^\infty \bar{k}(t)dt=\sum_{n=0}^{N}\frac{k_n}{\beta_n}\prod_{k=n+1}^{N}p_k\,, \tag{14}$$

$$\Sigma_{p_{tot}} = \bar{P}_{tot}+2\int_0^\infty \Sigma_{kt}(t)dt=\bar{P}_{tot}+\sum_{n=0}^{N}\sum_{j=0}^{n}\frac{k_n}{\beta_n}\frac{k_j}{\beta_j}\prod_{k=j+1}^{N}p_k-\bar{P}^2_{tot}\,. \tag{15}$$

The lower bound for the CV of the total number of P^* is

$$CV_{p_{tot}}=\frac{\sqrt{\Sigma_{p_{tot}}}}{\bar{P}_{tot}}\geq\frac{\sqrt{1+\frac{N}{\bar{P}_{tot}}}}{\sqrt{N}}\,. \tag{16}$$

Although the coefficient of variations $CV_{p_{tot}}$ and CV_τ share the same lower bound $1/\sqrt{N}$, in general, minimal values for both cannot be achieved simultaneously. Indeed, whereas a minimal $CV_{p_{tot}}$ requires $k_n/\beta_n=const$ and $p_n=1$, a minimal CV_τ is achieved for $1/\beta_n=const$ and $p_n=1$. Thus, by adjusting the activation rates k_n one can have a minimal $CV_{p_{tot}}$ even when CV_τ is far from being minimal. Thus, a reliable $R*$ lifetime is neither necessary nor sufficient for a reliable PDE activation. For constant transducin activation rates ($k_n=k$) we have almost linear relations $\bar{P}_{tot}=k\bar{\tau}$, $\Sigma_{p_{tot}}$ and $\Sigma_{p_{tot}}=\bar{P}_{tot}+k^2\Sigma_\tau$ (see also [15]).

2.4 Modeling the spontaneous PDE activation

In addition to PDE activation after a photon absorption, PDE molecules activate and deactivate spontaneously with Poisson rates ν_{sp} and μ_{sp} according to the biochemical reaction

$$P \underset{\mu_{sp}}{\overset{\nu_{sp}}{\rightleftharpoons}} P^*_{sp}\,. \tag{17}$$

Spontaneous PDE activation is an inconvenient mechanism, generating a background noise (dark noise) that obscures the signal from a single photon absorption: the signal generated by a photon has to overcome the dark noise amplitude[7]. However, spontaneous PDE activations are crucial because they hydrolyze cGMP in the dark and are essential to guarantee a steady-state concentration of cGMP in the transduction current in the dark.

Using Eq. 17, the average steady-state number of spontaneously activated PDE in a compartment is given by

$$\bar{P}^*_{sp,comp} = 2\rho_{pde}\pi R^2 \frac{\nu_{sp}}{\mu_{sp}}\,, \tag{18}$$

where ρ_{pde} is the PDE surface density and R is the compartment radius. For example, for toad rods, assuming $\nu_{sp} = 4 \times 10^{-4} s^{-1}$ and $\mu_{sp} = 1.8 s^{-1}$ [7], $R = 3\mu m$ and $\rho_{pde} = 100 \mu m^{-2}$ (see Table 3), we find $\bar{P}^*_{sp,comp} = 1.25$. Fig 2D shows a simulation of the stochastic number of spontaneously activated PDE in a mouse compartment with $\bar{P}^*_{sp,comp} = 0.9$ and $\mu_{sp} = 12.4 s^{-1}$ (see Table 3).

We use Eq. 17 together with the SSA Gillepie algorithm [17] to simulate the time course of the stochastic number of spontaneously activated PDE in a compartment (Fig 2D).

2.5 Homogenization of the three-dimensional ROS geometry and reduction of diffusion in a long cylinder

The outer segment (OS) is the sensory unit of the photoreceptor. The rod OS is divided by internal parallel disks into compartments connected to each other through narrow gaps between the disk rim and the OS membrane and through incisures (Fig. 3). A photon is absorbed by a rhodopsin photopigment attached to the surface of a single internal disk. As discussed in the previous paragraphs, Rhodopsin activation after a photon absorption triggers the activation of many PDE enzymes via a G-protein (transducin) coupled amplification cascade. Because PDE and transducin molecules are also attached to the disk surface, the activation process occurs on the internal disk surface, where the photon has been absorbed (Fig 2A). An activated PDE hydrolyzes (kill) the cytosolic second messenger cGMP that controls the opening of CNG ion channels in the OS membrane.

The compartmentalization of the OS restricts the diffusion of cGMP between neighbouring compartments, whereas diffusion within a compartment is not affected and leads to rapid transversal equilibration. We therefore adopt the approximation of a transversally well stirred OS where the three-dimensional geometry is reduced to an effective one-dimension model with an effective longitudinal diffusion constant [19, 20]. We now describe this geometrical reduction as shown in fig 3 and the estimation of the cGMP hydrolysis rate using a general Narrow Escape Theory [21] in a flat cylinder that involves two- and three-dimensional asymptotic estimates [14].

2.6 Computing the effective longitudinal diffusion constant

The model of diffusion reduction starts with considering Brownian particles in the OS, that are driven by thermal noise and a trajectory in the cytoplasmic fluid is well described by the overdamped approximation (Smoluchowski limit) of the Langevin equation. For a molecule located at position $X(t)$, the velocity satisfies the stochastic equation

$$\gamma \dot{X} + F(X) = \sqrt{2\gamma\varepsilon}\dot{\mathbf{w}} \tag{19}$$

where $F(x)$ are forces applied onto the particle, γ is the viscosity coefficient, $\varepsilon = \frac{kT}{m}$ is the thermal noise, and $\dot{w}$ is the white noise produced by thermal collisions [20, 22].

To study equation (19), we make three assumptions: 1) particles do not bind; 2) in the time scale of seconds, short range electrostatic interactions that arise from the charged disc membrane surfaces [23] and/or charged particles in solution average and cancel out. As a consequence all electrostatic terms are neglected and the force term $F(x)$ in eq. 19 is set to zero; 3) particles do not permeate across OS membranes.

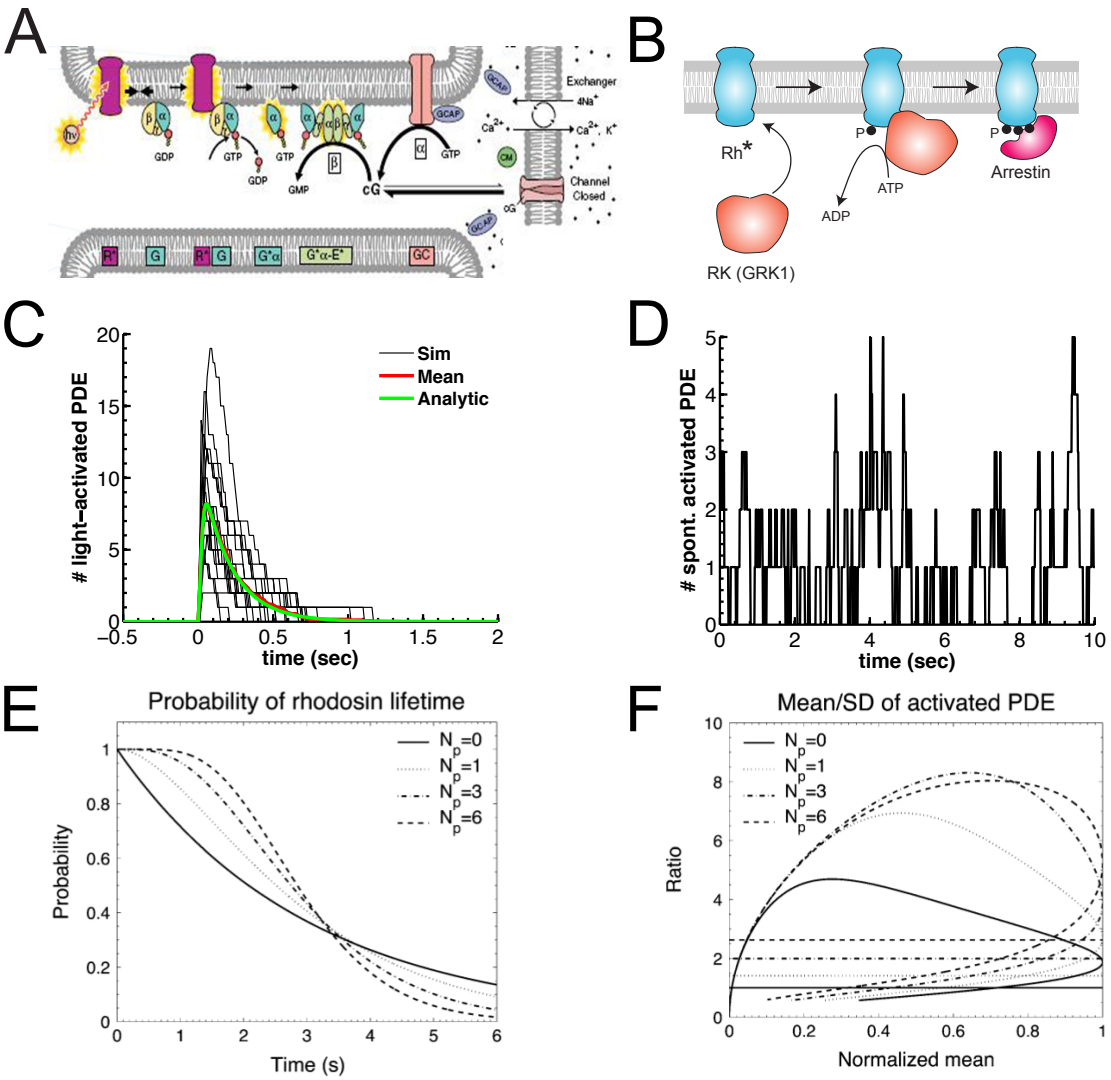

Fig. 2: **Signal transduction and PDE activation.** (A) Signal transduction cascade of a vertebrate photoreceptor. (B) Schematic representation of deactivation of an activated rhodopsin following multiple phosphorylations and arrestin binding [18]. (C) Stochastic simulations (black) of the number of activated PDEs after a single photon absorption in a mouse rod, average (red) and the analytic result for the mean (green). (D) Stochastic simulation of the number of spontaneously activated PDEs in a mouse compartment withe a mean $\bar{P}^*_{sp,comp} = 0.9$ and $\mu_{sp} = 12.4s^{-1}$. (E) Probability of activated rhodopsin lifetime depending on the number of phosphorylation sites. (F) Mean to standard-deviation ratio for activated PDEs plotted as a function of the mean PDE normalized by its maximum value [15].

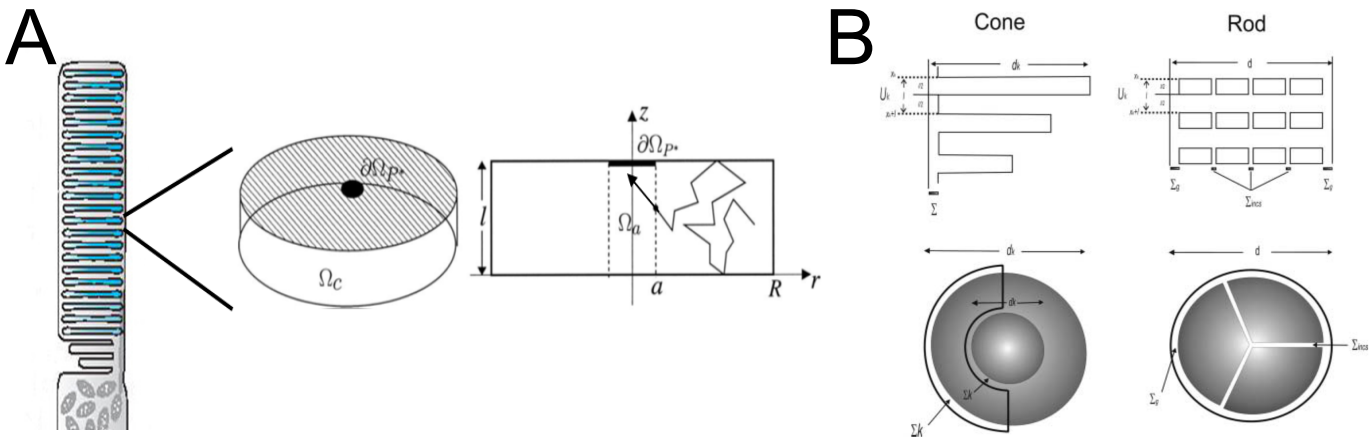

Fig. 3: **PDE hydrolysis rate and homogenization.** (A) Schematic representation of a cylindrical compartment with an activated PDE on the surface. A diffusing cGMP trajectory in the cytosol is terminated (hydrolyzed) when reaching the activated PDE site for the first time. (B) Schematic representation of cone and rod outer segment structure used to compute an effective longitudinal diffusion constant.

From the general theory of diffusion, it is well known that the probability density function (pdf) of one molecule associated with eq. 1 satisfies the standard three-dimensional diffusion equation inside the cytoplasmic fluid. Under the assumption of independent molecules, the concentration is simply the product of the pdf by the number of molecule and satisfies the diffusion equation within the OS:

$$\frac{\partial c}{\partial t} = D\Delta c \tag{20}$$

$$c(x,0) = c_0(x) \tag{21}$$

where $c_0(x)$ is some initial concentration, and D is the diffusion constant

2.7 Longitudinal diffusion in rod outer segments

ROS consists of repeating spatial compartments, U_k Fig.3B. Each compartment comprises the distance from one disc surface to the comparable surface in the next disc. The repeat distance is l, and it consists in two parts: the cytoplasmic space separating two adjacent discs (interdisc space, dimension=$l/2$) and the disc itself (dimension=$l/2$). Diffusion between adjacent interdisc spaces occurs either through disc incisures or the perimeter gap that separates disc edges from the plasma membrane. The compartments' radius is constant and denoted by r. We adopt the following notation: N_k is the number of free Brownian particles in the U_k compartment of volume V_k. The present analysis originates from [20].

The objective of the following derivation is to compute the ROS longitudinal diffusion constant, D_l, in terms of the OS's structure. Variation in the number of particles in unit U_k equals the difference of flux into compartments k-1 and k+1, that is

$$\frac{dN_k(t)}{dt} = -D[J_k - J_{k+1}] \tag{22}$$

By definition, J_{k+1} is the flux between unit U_k and U_{k+1} through Σ_{k+1}, the open surface that joins them,

$$J_{k+1} = \int_{\Sigma_{k+1}} \frac{\partial c(x,t)}{\boldsymbol{n}(x)} dS \tag{23}$$

where $\boldsymbol{n}(x)$ is the normal derivative pointing outside U_k and $\partial U_k = \Sigma_{k+1} \cup \Sigma_k$. In the time scale of seconds, the concentration is assumed to be uniform within each U_k compartment. This assumption is valid because: 1) diffusion within a compartment (transverse diffusion) is the standard two dimensional diffusion process where the diffusion constant equals to the aqueous diffusion constant; 2) the ratio of the absorbing boundary surface divided by the reflective boundary surface of a given compartment is small.

As a consequence, the diffusion along the longitudinal axis is much slower than along the transverse axis. Finally since the concentration inside a compartment equilibrates quickly at the time scale of seconds, the concentration can be considered to be uniform. Thus the flux through disk incisures and the perimeter gap is the same and does not depend on the transverse spatial variable.

Combining eqs. 22 and 23 yields,

$$\frac{1}{V_k}\frac{dN_k(t)}{dt} = \frac{D}{V_k}(n\Sigma_{incs} + \Sigma_g)(\frac{\partial c(x_{k+1},t)}{\partial x} - \frac{\partial c(x_k,t)}{\partial x}), \tag{24}$$

where Σ_{incs} is the surface area of a single disk incisures, n is the number of incisures and Σ_g is the surface of the perimeter gap between the disk's edge and plasma membrane. $\Sigma_g = 2\pi r g_w$, where r is the ROS radius and g_w is the size of the perimeter gap. The concentration at points $x_{k+1} = x_k + l$ and x_k is evaluated by a Taylor expansion. At the first order, since $c(x_k,t) = \frac{N_k(t)}{V_k}$, then

$$\frac{\partial c(x_k,t)}{\partial t} = \frac{1}{V_k}\frac{dN_k(t)}{dt} = \frac{D}{V_k}(n\Sigma_s + \Sigma_l) l \frac{\partial^2 c(x_k,t)}{\partial x_k^2}. \tag{25}$$

The translation invariance of the rod outer-segment geometry implies that the volume V_k of the compartment U_k is constant with respect to k and equals to the free interspace volume (free volume of the unit plus the free volume of the incisures)

$$V_k = \pi r_k^2 l/2 + nV_{incs} + V_g = \pi r^2 l/2 + (n\Sigma_s + 2\pi r g_w) l/2, \tag{26}$$

where V_{incs} is the volume of the incisure and V_g is the volume of the perimeter gap. Finally, eq. 25, can be reduced to the form of the standard one dimensional diffusion equation, for $x \in [0, L]$

$$\frac{\partial c(x,t)}{\partial t} = D_l \frac{\partial^2 c(x,t)}{\partial x^2}, \tag{27}$$

where the longitudinal diffusion constant is defined to be:

$$D_l = \frac{D(n\Sigma_{incs} + \Sigma_g) l}{\pi r^2 l/2 + (n\Sigma_{incs} + \Sigma_g) l/2} = 2D \frac{1}{\frac{\pi r^2}{n\Sigma_{incs} + \Sigma_g} + 1} \tag{28}$$

2.8 Longitudinal diffusion in cone outer segments (COS)

COS consists of repeating U_k compartments, each comprising the distance from the intracellular surface of one membrane fold to the intracellular surface of the next one (Fig 3B). The repeat distance

is l and it consists of two segments: the membrane fold (size=$l/2$) and the distance separating one fold from the next (size=$l/2$). The volume connecting adjacent folds can be very complicated, however in average, we can assume that the geometrical shape is fixed and well approximated by a cylinder of length=$l/2$and diameter δ.

To remember that δ is the diameter of a disk of area equal to the area of the real surface, we will refer to δ as the "equivalent diameter". The diameter of a fold at position x_k is denoted by d_k and it increases linearly with the longitudinal coordinate as given by $d_{k+1} = d_k + d_0$, where $d_0$is the incremental distance.

Derivation of the longitudinal diffusion equation in COS proceeds through the same steps as the derivation for ROS, but differs due the difference in the geometry. This difference is due to variation of the spatial compartment U_k. In COS, the time variation in the particle number in the U_k compartment is given by eq. 22 and the flux through the Σ_{k+1} surface is given by eq. 23. From these equations, the variation in time of the concentration in a COS compartment is given by:

$$\frac{1}{V_k}\frac{dN_k(t)}{dt} = \frac{1}{V_k}(D\Sigma_{k+1}\frac{\partial c(x_{k+1},t)}{\partial n(x)} - D\Sigma_k\frac{\partial c(x_k,t)}{\partial n(x)}) \tag{29}$$

Since $\Sigma_{k+1} = \Sigma_k$, using a Taylor expansion of the concentration c(x,t), we have:

$$\frac{\partial c(x_k,t)}{\partial t} = \frac{1}{V_k}\frac{dN_k(t)}{dt} = \frac{D\Sigma_{k+1}l}{V_k}\frac{\partial^2 c(x_k,t)}{\partial^2 x_k} \tag{30}$$

The area of the surface Σ_{k+1} is given by $\Sigma_{k+1} = \pi(\delta/2)^2$ and the volume is:

$$V_k = \pi(\delta/2)^2 l/2 + \pi(d_k/2)^2 l/2 \tag{31}$$

For $d_{\min}$ the smallest COS diameter (at its tip), d_{max} is the maximal COS diameter (at its base), L is the COS length

$$\alpha = \frac{d_{max} - d_{min}}{L} \tag{32}$$

Because of the cone geometry, at position x_k the cone diameter is $d_k = \alpha x_k + d_{\min}$, the longitudinal diffusion equation can now be expressed as:

$$\frac{\partial c(x_k,t)}{\partial t} = \frac{D\pi(\delta/2)^2 l}{\pi(\delta/2)^2 l/2 + l/8\pi(\alpha x_k + d_{\min})^2}\frac{\partial^2 c(x_k,t)}{\partial x_k^2} \tag{33}$$

for $x \in [0, L]$, the equation simplifies

$$\frac{\partial c(x,t)}{\partial t} = \frac{2D\delta^2}{\delta^2 + (x\alpha + d_{\min})^2}\frac{\partial^2 c(x,t)}{\partial x^2} \tag{34}$$

The longitudinal diffusion coefficient (which is now in one dimension a function of x) is explicitly given by

$$D(x) = \frac{2D\delta^2}{\delta^2 + (x\alpha + d_{min})^2}. \tag{35}$$

2.9 Determination of the diameter function $\delta(x)$ from the COS structure

Using the COS structure, equation 33 can be modified, to include a spatial dependency in the δ variable. Recall that the COS geometry is characterized by the following global parameters. L is the Length, r_{base} is the radius at the base, r_{tip} is the radius at the tip and $\alpha' = \frac{r_{base}-r_{tip}}{L}$. The surface $\Sigma_g(x)$ at the longitudinal position x, connecting adjacent folds is not circular, rather it is a semicircular disk that surrounds half the perimeter of the membrane folds over the entire COS length (Fig. 3B). Although by analyzing the electron Microscopy picture, $\Sigma_g(x)$ fluctuates along the OS, we will neglect such fluctuations compared to the mean.

If $r_m(x)$ is the radius up to the plasma membrane and $r_f(x)$ is the radius of the membrane fold at position x, the surface $\Sigma_g(x)$ (Fig. 3B) then the area of $\Sigma_g(x)$ is

$$\Sigma_g(x) = \frac{\pi}{2}(r_m(x)^2 - r_f(x)^2) \tag{36}$$

For $r_{tip} \leq r_f(x) \leq r_{base}$, $r_f(x) = r_{tip} + \alpha' x$ and $r_m(x) = r_f(x) + d$, the gap between the closed loop of a fold and the plasma membrane is about 100 Δ, that is $d = r_m - r_f$ =0.01 μ is small compare to r_m. We can approximate $\Sigma_g(x)$ by

$$\Sigma_g(x) = \pi d r_f(x) = \pi d(r_{tip} + (\frac{r_{base} - r_{tip}}{L})x) \tag{37}$$

Let us define the diameter function $\delta(x)$ of a disk along the COS of the same area as $\Sigma_g(x)$ by

$$\Sigma_g(x) = \pi(\delta(x)/2)^2 \tag{38}$$

then

$$\delta(x) = 2\sqrt{d(r_{tip} + \alpha' x)} \tag{39}$$

Using the result of the previous section, we can now incorporate the small changes in the diameter function $\delta(x)$ into the cone diffusion equation and equation (33) becomes

$$\frac{\partial c(x,t)}{\partial t} = \frac{2D\delta(x)^2}{\delta(x)^2 + (x\alpha + d_{\min})^2}\frac{\partial^2 c(x,t)}{\partial x^2} \tag{40}$$

with

$$\delta(x) = 2\sqrt{d(r_{tip} + \alpha x)} \tag{41}$$

An other derivation of this result using homogenization method can be found in [24].

3 Computing cGMP hydrolysis rates

Key parameters that control the CNG channel opening and the current response are the rates of cGMP hydrolysis by spontaneously and light-activated PDE, denoted by k_{sp} and k_{li} that we shall compute now.

3.1 Rate of hydrolysis by spontaneously activated PDE

The rate of cGMP hydrolysis by a spontaneously activated PDE k_{sp} is computed from formula [25, 19]

$$\beta_d = k_{sp}\bar{P}^*_{sp,comp}\,. \tag{42}$$

For example, for a toad rod with the experimental value $\beta_d = 1s^{-1}$ [16, 11] and $\bar{P}^*_{sp,comp} = 1.25$ [7] we find $k_{sp} \approx 0.8s^{-1}$. For a mouse rod with $\beta_d = 4.1s^{-1}$ [26] and $\bar{P}^*_{sp,comp} = 0.9$ (see further down) we get $k_{sp} = 4.5s^{-1}$ (Fig. 3). The different values of k_{sp} in toad and mouse might be due to the temperature, due to the different encounter rates between PDE and cGMP, or due to differences in the PDE enzyme between amphibians and mammals.

3.2 Computing the rate of hydrolysis by light-activated PDE from the Narrow Escape theory

Light-activated PDE is one of the most efficient enzymes [27]. As a consequence, cGMP hydrolysis by light-activated PDE is limited by the encounter rate k_{enc} between an activated PDE molecule diffusing on the disk surface and a cGMP molecule diffusing in the cytoplasms. Because cGMP diffusion in the cytoplasm is much faster than PDE diffusion in the membrane ($\sim 100\mu m^2/s^{-1}$ vs $0.8\mu m^2/s^{-1}$ [28], we can neglect PDE diffusion and assume that PDE is immobile. In that case, the mean rate hydrolysis rate is inversely proportional to the mean first passage time (MFPT) a cGMP molecule takes to find an activated PDE located on the surface of the compartment.

To estimate the encounter rate in a cylindrical compartment of radius R and height h, we compute the first passage time of a diffusing cGMP molecule to hit a circular spot of radius a located on the surface (Fig 3A). The radius a equals the reaction radius between activated PDE and cGMP. To derive analytic expressions, we place the activated PDE molecule at the disk center. This assumption will not much affect the leading order term, because in a two or three-dimensional space, the leading order term of the mean first passage time to a small surface target does not depend on the position of target [29]. The first passage time $\tau(r,z)$ (cylindrical coordinates with rotational symmetry) of a cGMP molecule initially at position (r,z) satisfies the mixed boundary value problem [30]

$$\begin{aligned} D_g\Delta\tau(r,z) &= -1\,, \quad 0<z<h\,, 0\le r<R \\ \tau(r,z) &= 0\,, \quad z=0\,, r\le a \\ \frac{\partial}{\partial z}\tau(r,z) &= 0\,, \quad z=0\,, r>a \text{ and } z=h \\ \frac{\partial}{\partial r}\tau(r,z) &= 0 \quad r=R \end{aligned} \tag{43}$$

D_g is the cGMP diffusion coefficient. To obtain the MFPT $\bar{\tau}$, we average the solution $\tau(r,z)$ over a uniform initial distribution. The result is [25]

$$k_{enc} = \frac{1}{\bar{\tau}} = \frac{D_g}{R^2}\left(\pi\frac{h}{a}\frac{a_0(h/a)}{\sqrt{2}} + \frac{4\ln(R/a)-3}{8}\right)^{-1}, \tag{44}$$

where the function $a_0\left(\frac{h}{a}\right)/\sqrt{2} \in [0.07, 0.25]$ is shown in (fig 2a of [14]. When $h \sim R$, $a_0(\frac{h}{a}) \sim \frac{1}{4}$. We note that the log-contribution in expression originates from the degenerated geometry (flat cylinder). An analytic closed representation of the function a_0 is unknown.

We recall that general expression of the MFPT $\bar{\tau}$ depends on the initial position in the dimensionless variables

$$x = \frac{r}{a}\,, \quad y = \frac{z}{a}\,, \quad \alpha = \frac{R}{a}\,, \quad \beta = \frac{h}{a}\,, \quad |\Omega| = \frac{|V|}{a^3} = \pi\beta\alpha^2\,,$$

is

$$\hat{\tau}(x,y) = \begin{cases} \displaystyle\sum_{n=0}^{\infty} b_n \frac{I_0(l_n x)}{I_0(l_n)} v_n(y) + w_i(x,y)\,, & x \le 1 \\ \\ \displaystyle = \sum_{n=0}^{\infty} a_n \frac{F_0(k_n x, k_n \alpha)}{F_0(k_n, k_n \alpha)} u_n(y) + \frac{\ln x}{2\pi\beta} - \frac{x^2-1}{4|\Omega|}\,, & 1 \le x \le \alpha, \end{cases} \tag{45}$$

where

$$\begin{gathered} u_0 = \frac{1}{\sqrt{2}}\,, \quad u_n(y) = \cos(k_n y) \quad (n \ge 1)\,, \quad v_n(y) = \sin(l_n y) \quad (n \ge 0)\,, \\ k_n = \frac{n\pi}{\beta}\,, \quad l_n = \frac{(n+\frac{1}{2})\pi}{\beta} \end{gathered} \tag{46}$$

and the modified Bessel functions are $I_0(x)$ and $K_0(x)$ and the relations [31] ($I_0'(x) = I_1(x)$, $K_0'(x) = -K_1(x)$, we obtain

$$p_n(x) = \frac{F_0(k_n x, k_n \alpha)}{F_0(k_n, k_n \alpha)}\,, \tag{47}$$

with

$$F_0(x,y) = I_0(x)K_1(y) + K_0(x)I_1(y)\,.$$

We recall that

$$\begin{aligned} w_i(x,y) &= \frac{1}{|\Omega|} \sum_{n=1}^{\infty} c_n J_0(z_n x) \frac{\cosh(z_n(\beta - y))}{\cosh(z_n \beta)} - \frac{x^2-1}{4|\Omega|} \\ &= \frac{1}{|\Omega|} \sum_{n=1}^{\infty} c_n J_0(z_n x) \left(\frac{\cosh(z_n(\beta - y))}{\cosh(z_n \beta)} - 1 \right)\,, \end{aligned} \tag{48}$$

where z_n are the positive zeros of the Bessel function $J_0(x)$, and the coefficients c_n are given by

$$c_n = \frac{2}{J_0'(z_n)^2} \int_0^1 J_0(z_n x) \frac{x^2-1}{4} x dx\,. \tag{49}$$

With the relation

$$\alpha_0 = 0\,, \quad \alpha_n = -k_n \frac{F_1(k_n, k_n\alpha)}{F_0(k_n, k_n\alpha)} \ (n \ge 1)\,, \quad \beta_n = l_n \frac{I_1(l_n)}{I_0(l_n)} \tag{50}$$

we obtain a closed matrix equations for the coefficient a_n and b_n

$$\begin{aligned} \sum_{m=0}^{\infty} (\beta_n + \alpha_m) \xi_{nm} a_m &= \sum_{m=0}^{\infty} \xi_{nm} \gamma_m \\ \sum_{m=0}^{\infty} (\beta_m + \alpha_n) \xi_{mn} b_m &= \gamma_n\,. \end{aligned} \tag{51}$$

where

$$\xi_{nm} = \begin{cases} \dfrac{2}{\beta}\dfrac{l_n}{l_n^2 - k_m^2} = \dfrac{2}{\pi}\dfrac{(n+\frac{1}{2})}{(n+\frac{1}{2})^2 - m^2}\,, & m \geq 1 \\ \\ \dfrac{\sqrt{2}}{\beta l_n} = \dfrac{\sqrt{2}}{\pi}\dfrac{1}{n+\frac{1}{2}}\,, & m = 0 \end{cases} \tag{52}$$

is an orthogonal matrix. It is possible to solve these matrix equations by truncating the system at a certain n leading to an approximated solution for a_n resp. b_n. This will lead to an approximation for the NET $\hat{\tau}(x, y)$ [14].

The encounter rate is given by relation 44 and clarifies how it depends on the underlying geometrical and diffusion properties. For example, for a toad rod with $R = 3\mu m$ we compute $k_{enc} \approx 2.9s^{-1}$, and for a mouse with $R = 0.7\mu m$ we find $k_{enc} \approx 61s^{-1}$ (with $a = 3nm$, $h = 15nm$ and $a_0(h/a) \approx 0.7$). As it turn out, the dependency of k_{enc} on the OS geometry is crucial to understand how many activated PDE are necessary to generate a signal that overcomes the noise. For mouse, the calculated rate $k_{enc} = 61s^{-1}$ for mouse is close to the vaue $43s^{-1}$ extracted from experimental data [26].

4 Modeling the dynamics of cGMP and calcium ions

4.1 Coarse-grained model for cGMP dynamics

This part of the model consists in first considering separately the dynamics occurring in each compartment: synthesis and hydrolysis of cGMP and second to couple cGMP to neighboring compartments through the reduced diffusion derived in paragraph 2.6.

The biochemistry can be described as follows: cGMP synthesis is catalyzed by guanylyl cyclase (GC) that are uniformly distributed on the surface of the disks. The synthesis rate depends on calcium through Ca^{2+}-sensitive guanylyl cyclase activating proteins (GCAPs) that inhibit GC at high Ca^{2+} concentration [32, 33, 34, 35]. The calcium dependent cGMP synthesis rate in compartment n is described by the function

$$\alpha_s(n,t) = \alpha_{max}\left(r_\alpha + (1-r_\alpha)\frac{K_\alpha^{n_\alpha}}{K_\alpha^{n_\alpha} + c(n,t)^{n_\alpha}}\right)\,, \tag{53}$$

where $c(n,t)$ is the free Ca^{2+} concentration in compartment n, α_{max} is the maximal synthesis rate for low free calcium, $r_\alpha = \frac{\alpha_{min}}{\alpha_{max}}$ is the ratio between minimal and maximal synthesis rate, K_α is the calcium concentration for which the synthesis rate is $(\alpha_{max} + \alpha_{min})/2$, and n_α is the Hill coefficient.

The rate of cGMP hydrolysis depends on the number of spontaneously activated PDE $P_{sp}^*(n,t)$ and the number of light-activated PDE $P_{li}^*(n,t)$,

$$\alpha_h(n,t) = k_{sp}P_{sp}^*(n,t) + k_{li}P_{li}^*(n,t)\,. \tag{54}$$

k_{sp} is the rate constant for a single spontaneously activated PDE, and k_{li} the diffusion limited rate constant for light activated PDE, for which we use the encounter rate computed in Eq. 44.

The longitudinal cGMP diffusion between compartments occurs through the effective longitudinal diffusion constant $D_{g,l} < D_g$, where D_g is the fast cytosolic diffusion constant [20]. By applying Ficks law to model the longitudinal flux between neighboring compartments separated by the distance $h+w$ (compartment height plus disk width) we get the discrete flux

$$j_{d,g}(n,t) = \frac{D_{g,l}}{h(h+w)}(g(n+1,t) + g(n-1,t) - 2g(n,t))\,, \tag{55}$$

where $g(n,t)$ is the cGMP concentration in compartment n. Finally, the dynamics of cGMP across the ROS satisfies the equation

$$\frac{d}{dt}g(n,t) = j_{d,g}(n,t) + \alpha(n,t) - \left(k_{sp}P^*_{sp}(n,t) + k_{li}P^*_{li}(n,t)\right) g(n,t)\,. \tag{56}$$

4.2 Reduced model for calcium dynamics

To model Ca^{2+} dynamic, we take into account the effective longitudinal diffusion between compartments, the exchange between the OS and the extracellular medium through cGMP gated channels and $Ca^{2+}Na^{+}K^{+}$ exchangers, and the buffering activity. The model is presented now.

4.3 Modeling calcium buffers

In darkness, there a steady state concentration of free calcium $c_d \approx 0.3\mu M$ [36] that corresponds on average to ~ 3.3 ions in a compartment. This number is surprisingly small, given that many feedback process are regulated by Ca^{2+}. However, there are many Ca^{2+} binding proteins in the OS that contribute to buffer calcium and increase the amount of Ca^{2+} present in the OS, e.g recoverin, GCAPs and calmodulin. For example, the concentration of recoverin in a mammalian rod is $\sim 600\mu M$ [36], around 2000 times larger than the free calcium concentration; and the GC membrane concentration $\sim 50\mu m^{-2}$ [36] corresponds to ~ 150 enzymes in a mouse compartment, around 40 times more than the number of free calcium ions.

In that model, we use the simplest buffering scenario: the buffering activity is much faster than the time scale where the free Ca^{2+} concentration fluctuates, and we use a linear relation between buffered and free Ca^{2+}, valid if the amount of buffered Ca^{2+} is small compared to the total buffer capacity. Hence, we consider that the number of bound calcium is

$$c_b(n,t) = B_{ca}c(n,t) \tag{57}$$

with the buffering capacity is B_{ca}.

4.4 Dynamics of calcium exchange via channels and exchangers

Free internal Ca^{2+} ions are exchanged between the OS and the extracellular medium through cGMP gated channels and $Ca^{2+}Na^{+}K^{+}$ exchangers. The Ca^{2+} influx through the CNG channels depends on the probability $p_{ch}(n,t)$ that a channel is open, which is a function of the local cGMP concentration:

$$p_{ch}(n,t) = \frac{g(n,t)^{n_{ch}}}{g(n,t)^{n_{ch}} + K_{ch}^{n_{ch}}}\,. \tag{58}$$

The $Ca^{2+}-$efflux through exchangers depends on the free concentration $c(n,t)$ and the exchanger saturation level, leading to the relation

$$p_{ex}(n,t) = \frac{c(n,t)}{c(n,t) + K_{ex}}. \tag{59}$$

The net local Ca^{2+} membrane flux is

$$J_{ca}(n,t) = J_{ch,ca}(n,t) + J_{ex,ca}(n,t) = J_{ch,ca,max}p_{ch}(n,t) + J_{ex,ca,max}p_{ex}(n,t)\,. \tag{60}$$

The inward current through the CNG channels is carried by both ions Na^+ and Ca^{2+}

$$I_{ch}(n,t) = I_{ch,na}(n,t) + I_{ch,ca}(n,t) = \frac{I_{ch,ca}(n,t)}{f_{ca}} = -\frac{2\mathcal{F}J_{ch,ca}(n,t)}{f_{ca}}\,, \tag{61}$$

where $\mathcal{F}$ is the Faraday constant. There is only a fraction $f_{ca} \sim 0.1 - 0.15$ of the channel current carried by Ca^{2+} ions [36]. The extrusion of a single Ca^{2+} ion by the exchanger is accompanied by the influx of four Na^+ ions and the efflux of one K^+ [37]. Thus, the extrusion of one Ca^{2+} leads to the influx of a single positive charge, producing the net exchanger current

$$I_{ex}(n,t) \quad = \mathcal{F}J_{ex,ca}(n,t)\,. \tag{62}$$

Using Eq. 61 and Eq. 62, we obtain for the local current

$$I(n,t) = I_{ch}(n,t) + I_{ex}(n,t) = \mathcal{F}\left(-\frac{2}{f_{ca}}J_{ch,ca}(n,t) + J_{ex,ca}(n,t)\right) \tag{63}$$

(see below for the analytical expressions). At steady-state in darkness, the calcium influx and efflux are balanced thus

$$J_{ch,ca}(n) + J_{ex,ca}(n) = 0. \tag{64}$$

From Eq. 63, we obtain the expression for the dark current associated with a single compartment

$$I_{comp,d} = -\mathcal{F}\left(\frac{2}{f_{ca}} + 1\right) J_{ch,ca,comp,d} = \mathcal{F}\left(\frac{2}{f_{ca}} + 1\right) J_{ex,ca,comp,d}\,. \tag{65}$$

We can use this result to express the calcium fluxes as a function of $I_{comp,d}$,

$$\begin{aligned} J_{ch,ca}(n,t) &= J_{ch,ca,comp,d}\frac{J_{ch,ca}(n,t)}{J_{ch,ca,comp,d}} = -\frac{I_{comp,d}}{\mathcal{F}}\frac{f_{ca}}{f_{ca}+2}\frac{p_{ch}(n,t)}{p_{ch,d}} \\ J_{ex,ca}(n,t) &= J_{ex,ca,comp,d}\frac{J_{ex,ca}(n,t)}{J_{ex,ca,comp,d}} = \frac{I_{comp,d}}{\mathcal{F}}\frac{f_{ca}}{f_{ca}+2}\frac{p_{ex}(n,t)}{p_{ex,d}}\,, \end{aligned} \tag{66}$$

where g_d and c_d are the mean concentrations in darkness and

$$p_{ch,d} = \frac{g_d^{n_{ch}}}{g_d^{n_{ch}} + K_{ch}^{n_{ch}}} \quad \text{and} \quad p_{ex,d} = \frac{c_d}{c_d + K_{ex}}. \tag{67}$$

Using Eq. 66 in Eq. 60 we obtain

$$J_{ca}(n,t) = V_{comp}\phi\left(\frac{p_{ch}(t)}{p_{ch,d}} - \frac{p_{ex}(t)}{p_{ex,d}}\right)\,, \tag{68}$$

where we use the notation to connect to each compartment: $I_{os,d} = N_{comp}I_{comp,d}$, $V_{os} = N_{comp}V_{comp}$ and

$$\phi = \frac{f_{ca}}{f_{ca}+2}\frac{|I_{comp,d}|}{V_{comp}\mathcal{F}} = \frac{f_{ca}}{f_{ca}+2}\frac{|I_{os,d}|}{V_{os}\mathcal{F}}\,. \tag{69}$$

For example, in a mouse rod with a dark current $I_{os,d} = 16pA$ and a cytosolic volume $V_{os} \approx 18\mu m^3 = 18 \times 10^{-15} l$ [36] we find $\phi \approx 500\frac{\mu M}{s} = 0.5\frac{\mu M}{ms}$.

4.5 Mass-action equation for the free Ca^{2+} concentration

The longitudinal calcium diffusion proceeds with an effective diffusion constant $D_{c,l}$. By considering buffering and the diffusion exchanges, we obtain for the free calcium concentration the equation

$$\frac{d}{dt}c(n,t) = j_{d,c}(n,t) + \frac{\phi}{B_{ca}+1}\left(\frac{p_{ch}(t)}{p_{ch,d}} - \frac{p_{ex}(t)}{p_{ex,d}}\right). \tag{70}$$

with the exchange rate

$$j_{d,c}(n,t) = \frac{1}{B_{ca}+1}\frac{D_{c,l}}{h(h+w)}(c(n+1,t)+c(n-1,t)-2c(n,t)), \tag{71}$$

4.6 Coupled system of equations for cGMP and calcium currents

We scale the various quantities using the mean dark concentrations g_d and c_d

$$\begin{aligned} \hat{g}(n,t) &= \frac{g(n,t)}{g_d}, \quad \hat{ca}(n,t) = \frac{c(n,t)}{c_d}, \\ k_\alpha &= \frac{K_\alpha}{c_d}, \quad k_{ex} = \frac{K_{ex}}{c_d}, \quad k_{ch} = \frac{K_{ch}}{g_d}. \end{aligned} \tag{72}$$

The equations for the scaled cGMP and Ca^{2+} concentrations are

$$\begin{aligned} \frac{d\hat{g}(n,t)}{dt} &= j_{d,g}(n-1,n,n+1,t) + \beta_d \frac{r_\alpha + (1-r_\alpha)\dfrac{k_\alpha^{n_\alpha}}{k_\alpha^{n_\alpha}+\hat{c}(n,t)^{n_\alpha}}}{r_\alpha + (1-r_\alpha)\dfrac{k_\alpha^{n_\alpha}}{k_\alpha^{n_\alpha}+1}} - \left(k_{sp}P^*_{sp}(n,t) + k_{li}P^*_{li}(n,t)\right)\hat{g}(n,t) \\ \frac{d\hat{c}(n,t)}{dt} &= j_{d,c}(n-1,n,n+1,t) + \gamma_d\left(\frac{p_{ch}(n,t)}{p_{ch,d}} - \frac{p_{ex}(n,t)}{p_{ex,d}}\right). \end{aligned} \tag{73}$$

with

$$\begin{aligned} \beta_d &= k_{sp}\bar{P}^*_{sp,comp} \\ \frac{p_{ch}(n,t)}{p_{ch,d}} &= \frac{1+k_{ch}^{n_{ch}}}{\hat{g}(n,t)^{n_{ch}}+k_{ch}^{n_{ch}}}\hat{g}(n,t)^{n_{ch}} \\ \frac{p_{ex}(n,t)}{p_{ex,d}} &= \frac{1+k_{ex}}{\hat{c}(n,t)+k_{ex}}\hat{c}(n,t), \\ \gamma_d &= \frac{1}{B_{ca}+1}\frac{\phi}{c_d} = \frac{1}{B_{ca}+1}\frac{f_{ca}}{f_{ca}+2}\frac{|I_{os,d}|}{c_d V_{os}\mathcal{F}}. \\ j_{d,g}(n-1,n,n+1,t) &= \frac{D_{g,l}}{h(h+w)}\left(\hat{g}(n+1,t)+\hat{g}(n-1,t)-2\hat{g}(n,t)\right) \\ j_{d,c}(n-1,n,n+1,t) &= \frac{1}{B_{ca}+1}\frac{D_{c,l}}{h(h+w)}\left(\hat{c}(n+1,t)+\hat{c}(n-1,t)-2\hat{c}(n,t)\right) \end{aligned} \tag{74}$$

By inserting Eq. 66 into Eq. 63, we obtain the normalized current

$$\hat{I}(n,t) = \frac{I_{comp,d}-I(n,t)}{I_{comp,d}} = 1 - \frac{2}{f_{ca}+2}\frac{p_{ch}(n,t)}{p_{ch,d}} + \frac{f_{ca}}{f_{ca}+2}\frac{p_{ex}(n,t)}{p_{ex,d}}. \tag{75}$$

The overall normalized current from N_{comp} compartments is

$$\hat{I}_{os}(t) = \frac{I_{os,d}-I_{os}(t)}{I_{os,d}} = 1 - \frac{1}{I_{os,d}}\sum_{n=1}^{N_{comp}} I(n,t) = 1 - \frac{1}{N_{comp}}\sum_{n=1}^{N_{comp}} \hat{I}(n,t). \tag{76}$$

The parameter of the simulations are summarized in table 2:

Table 2: Parameters for the photocurrent simulation

Parameter	**Definition**
N_{comp}	Number of compartments
R	OS radius
h	Compartment height
w	Disk width
a	Reaction radius for cGMP hydrolysis by an activated PDE molecule
k_{enc}	Encounter rate between a cGMP and an activated PDE molecule
k_{li}	Rate constant for cGMP hydrolysis by a light-activated PDE
k_{sp}	Rate constant for cGMP hydrolysis by a spontaneous activated PDE Determined from the equation $\beta_d = k_{sp}\bar{P}^*_{sp,comp}$
β_d	cGMP hydrolysis rate in the dark
g_d	cGMP concentration in the dark
c_d	Free calcium concentration in the dark
$I_{os,d}$	OS current in the dark
f_{ca}	Fraction of current carried by calcium
B_{ca}	Buffering capacity for calcium
K_α	Michaelis constant for cGMP synthesis
K_{ch}	Michaelis constant for channel opening
K_{ex}	Michaelis constant for calcium exchanger
n_α	Hill coefficient for cGMP synthesis
r_α	Ratio of minimal to maximal cGMP synthesis rate
n_{ch}	Hill coefficient for channel opening
D_g	Radial cGMP diffusion constant
D_{ca}	Radial calcium diffusion constant
$D_{g,l}$	Effective longitudinal cGMP diffusion constant
$D_{ca,l}$	Effective longitudinal calcium diffusion constant
γ_d	Rate for calcium exchange

5 Stochastic simulations of the dark noise and the single photon response (SPR)

We now describe the simulation method of the SPR with dark noise[38]. For each compartment, we use the SSA algorithm [17] to generate spontaneously activated PDE $P^*_{sp}(n,t)$ from Poisson activation and deactivation rates ν_{sp} and μ_{sp}. To model the single-photon response, we simulated the number of light-activated PDE $P^*_{li}(t)$ in the compartment where a photon is absorbed. For simplicity, we assume that a photon is absorbed at the center of the outer segment. However, a different location would not have a significant effect on the results. Finally, the functions $P^*_{sp}(n,t)$ and $P^*_{li}(t)$ are input to the system of equations for calcium and cGMP Eq. 73, from which we can compute the normalized currents $\hat{I}(n,t)$ and $\hat{I}_{os}(t)$.

Combining all previous results into an integrated model, we can simulate a single-photon response with intrinsic noise. We present 20 single-photon responses (Fig. 4A) obtained from suction electrode-recordings in a WT mouse rod that we used to validate the model. Suction-electrode recording are used because cells could be held for longer times with this method, making it possible to obtain sufficient data from single cells over a period of several minutes. The data in Fig. 4A are representative of recordings from 8 rods, which all gave similar results. To generate the calculated single-photon response curves shown in Fig. 4B, we used simulations of light-activated PDE from Fig. 2C.

Under the experimental recording conditions, the decay time of light-activated PDE is about 200ms [39, 40], and the mean lifetime of excited rhodopsin is of the order of 40 ms [41, 39]. Furthermore, to reconcile the experimental and simulated response amplitude, we increased the transducin activation rates by a factor 1.75 compared to the toad simulations shown in Fig. 4B, which could be a result of the higher body temperature [42]. In addition, following this procedure, the average number of light-activated PDE increases from a value around 6 to around 8.2. The simulated responses in Fig. 4B show good agreement with the experimental recordings in Fig. 4A; however, the simulated dark noise ($\Sigma_{sim} = 2.3\%$) is higher compared to the recorded dark noise ($\Sigma_{dark} = 1.6\%$). A strong calcium feedback with no buffering ($B_{ca} = 1$) and no saturation in cGMP synthesis at high calcium concentrations ($r_\alpha = 0$) reduces both the noise level and the peak amplitude by around 50% [38].

6 Statistical analysis and parameter estimations

The current fluctuations in darkness (absence of photon) generate a noise called dark noise, the parameters of which can be extracted from the analytical expression of the power spectrum. We derive here such expression by considering that the dark noise is generated by the spontaneous activations and deactivations of PDE. From the expression of the dark noise, we estimate the spontaneous PDE activation process from electrophysiological recordings in the absence of photon response.

Using the model presented in the the previous section, in darkness there not light activated PDE thus $P^*_{li}(n,t) = 0$. The average value of the scaled quantities CGMP and calcium $\hat{g}(n,t)$, $\hat{c}(n,t)$ and $\hat{I}(n,t)$ is one. Using a linear noise expansion of the Fourier transform of Eq. 73, we obtain

$$\delta\hat{c}(\omega) = \sum_{n=1}^{N_{comp}} \delta\hat{c}(n,\omega) = \frac{\gamma_d}{\gamma_d\xi_{ex} - i\omega}\xi_{ch}\delta\hat{g}(\omega)\,, \tag{77}$$

$$\delta\hat{g}(\omega) = \sum_{n=1}^{N_{comp}} \delta\hat{g}(n,\omega) = \frac{\beta_d}{\beta_d - i\omega - \beta_d\xi_\alpha\frac{\gamma_d\xi_{ch}}{\gamma_d\xi_{ex}-i\omega}} \sum_{n=1}^{N_{comp}} \delta\hat{P}^*_{sp}(n,\omega)\,. \tag{78}$$

with

$$\xi_\alpha = -n_\alpha \frac{1}{k_\alpha^{n_\alpha}+1} \frac{(1-r_\alpha)\frac{k_\alpha^{n_\alpha}}{k_\alpha^{n_\alpha}+1}}{r_\alpha + (1-r_\alpha)\frac{k_\alpha^{n_\alpha}}{k_\alpha^{n_\alpha}+1}}\,, \quad \xi_{ch} = n_{ch}\frac{k_{ch}^{n_{ch}}}{1+k_{ch}^{n_{ch}}}\,, \quad \xi_{ex} = \frac{k_{ex}}{1+k_{ex}} \tag{79}$$

The overall current fluctuation (Eq. 76) is

$$\begin{aligned} \delta\hat{I}_{os}(\omega) &= \frac{1}{N_{comp}}\left(\frac{2}{f_{ca}+2} + \frac{f_{ca}}{f_{ca}+2}\frac{\gamma_d\xi_{ex}}{\gamma_d\xi_{ex}-i\omega}\right)\xi_{ch}\delta\hat{g}(\omega) \\ &= \chi_I(\omega)\frac{1}{N_{comp}}\sum_{n=1}^{N_{comp}}\delta\hat{P}^*_{sp}(n,\omega) \end{aligned} \tag{80}$$

where the transfer function is defined by

$$\begin{aligned} \chi_I(\omega) &= \left(1+\frac{f_{ca}}{f_{ca}+2}\frac{i\omega}{\gamma_d\xi_{ex}-i\omega}\right)\frac{\xi_{ch}\beta_d}{\beta_d\left(1-\frac{\gamma_d^2\xi_\alpha\xi_{ch}\xi_{ex}}{\gamma_d^2\xi_{ex}^2+\omega^2}\right)-i\omega\left(1+\frac{\beta_d\gamma_d\xi_\alpha\xi_{ch}}{\gamma_d^2\xi_{ex}^2+\omega^2}\right)} \\ &\approx -\frac{\xi_{ch}\beta_d}{\beta_d\left(1-\frac{\gamma_d^2\xi_\alpha\xi_{ch}\xi_{ex}}{\gamma_d^2\xi_{ex}^2+\omega^2}\right)-i\omega\left(1+\frac{\beta_d\gamma_d\xi_\alpha\xi_{ch}}{\gamma_d^2\xi_{ex}^2+\omega^2}\right)}. \end{aligned} \tag{81}$$

Because PDE activations in different compartments are independent, the spectrum of the overall scaled current $\hat{I}_{os}(t)$ is computed from the Lorentzian of a Poisson process (see section2.4):

$$S_{\hat{I}_{os}}(\omega) = |\chi_I(\omega)|^2\frac{1}{N_{comp}}\hat{S}_{P^*_{sp}} = \frac{1}{N_{comp}}\frac{|\chi_I(\omega)|^2}{P^*_{sp,comp}}\frac{4\mu_{sp}}{\mu_{sp}^2+\omega^2} = \frac{|\chi_I(\omega)|^2}{P^*_{sp,os}}\frac{4\mu_{sp}}{\mu_{sp}^2+\omega^2}\,. \tag{82}$$

The current variance is defined by

$$\Sigma_{\hat{I}_{os}} = \frac{1}{2\pi}\int_0^\infty S_{\hat{I}_{os}}(\omega)d\omega\,. \tag{83}$$

6.1 Power spectrum and variance for the mutant GCAPs$^{-/-}$ rod

In the mutant mice GCAPs$^{-/-}$, the $Ca^{2+}-$feedback on cGMP synthesis is abolished, which can be modeled by setting $n_\alpha = 0$ in Eq. 73. With $\xi_\alpha = 0$, the expression for $\chi_I(\omega)$ in Eq. 81 simplifies to

$$\chi_I(\omega) = -\frac{\xi_{ch}\beta_d}{\beta_d - i\omega}\,. \tag{84}$$

In that case, the power spectrum and variance of the scaled current reduce to

$$S_{\hat{I}_{os},gcap}(\omega) = \frac{4\xi_{ch}^2}{\bar{P}^*_{sp,os}\mu_{sp}}\frac{\beta_d^2\mu_{sp}^2}{(\beta_d^2+\omega^2)(\mu_{sp}^2+\omega^2)} \tag{85}$$

$$\Sigma_{\hat{I}_{os},gcap} = \frac{\xi_{ch}^2}{\bar{P}^*_{sp,os}}\frac{1}{1+\frac{\mu_{sp}}{\beta_d}} = \frac{\xi_{ch}^2}{N_{comp}\bar{P}^*_{sp,comp}}\frac{1}{1+\frac{\mu_{sp}}{\beta_d}}\,. \tag{86}$$

With the parameter values for mouse given in Table 4, we obtain $\Sigma_{\hat{I}_{os},gcap} \approx 0.055$, which agrees with the value 0.056 extracted from the GCAPs$^{-/-}$ simulations [38]. Various parameters are given in table 3 below:

Table 3: Parameters used to simulate PDE activation

Parameter	**Toad**	**Mouse**
$\bar{P}^*_{sp,comp}$	1.25	0.9
$\bar{P}^*_{li,max}$	150	8.2
$\mu_{sp}(\mathrm{s}^{-1})$	1.8	12.4
$\mu_p\ (\mathrm{s}^{-1})$	0.625	5
$\tau_{rh}\ (\mathrm{s})$	3	0.04
N	6	6
$k_N\ (\mathrm{s}^{-1})$	200	350
ω	0.1	0.1
$\mu_t\ (\mathrm{s}^{-1})$	300	300

6.2 Power spectrum and variance with fast calcium dynamics

The role of calcium feedback on cGMP synthesis is to reduce the current fluctuations. This feedback is efficient when the calcium dynamics is fast compared to the underlying PDE fluctuations, such that calcium changes can be used to monitor the PDE changes.

To estimate how much feedback reduces the current variance, we derive analytic expressions for the fast calcium dynamics that we compare to the ones for GCAPs$^{-/-}$ rods with no calcium feedback. For example, in a mouse rod, the rate constant γ_d governing the calcium dynamics in Eq. 73 has a value $\gamma_d \approx 1670 s^{-1}$ (Eq. 74 with no buffering, $B_{ca} = 1$). Adding buffers ($B_{ca} > 1$) slows down the dynamics and reduces the feedback.

For $\gamma_d \gg \frac{\omega}{\xi_{ex}}$ and $\gamma_d \gg \beta_d \xi_\alpha \xi_{ch}$ Eq. 81 simplifies to

$$\chi_I(\omega) \approx -\frac{1}{\zeta}\frac{\xi_{ch}\tilde{\beta}_d}{\tilde{\beta}_d - i\omega} \quad \text{with} \quad \zeta = 1 - \frac{\xi_\alpha \xi_{ch}}{\xi_{ex}} \quad \text{and} \quad \tilde{\beta}_d = \beta_d \zeta\,. \tag{87}$$

The spectrum and variance of the dark noise with fast calcium dynamics is te product of two Lorenzians:

$$S_{\hat{I}_{os},fast\,Ca}(\omega) = \frac{1}{\zeta^2}\frac{4\xi^2_{ch}}{\bar{P}^*_{sp,os}\mu_{sp}}\frac{\tilde{\beta}^2_d\mu^2_{sp}}{(\tilde{\beta}^2_d+\omega^2)(\mu^2_{sp}+\omega^2)} \tag{88}$$

$$\Sigma_{\hat{I}_{os},fast\,Ca} = \frac{1}{\zeta^2}\frac{\xi^2_{ch}}{\bar{P}^*_{sp,os}}\frac{1}{1+\frac{\mu_{sp}}{\tilde{\beta}_d}}\,. \tag{89}$$

Compared to GCAPs$^{-/-}$ rods, calcium feedback reduces the amplitude of the dark noise by a factor

$$\rho = \sqrt{\frac{\Sigma_{\hat{I}_{os},gcap}}{\Sigma_{\hat{I}_{os}fast\,Ca}}} = \zeta\sqrt{\frac{1+\frac{\mu_{sp}}{\tilde{\beta}_d}}{1+\frac{\mu_{sp}}{\beta_d}}}\,. \tag{90}$$

With mouse parameters from Table 4 we obtain $\rho \approx 2.5$ with $B_{ca} = 80$ and $r_\alpha = 0.066$, and $\rho \approx 4.4$ with strong feedback achieved for $B_{ca} = 0$ and $r_\alpha = 0$. From experimental recordings and dark noise simulations shown in Fig 4 and Fig 5, we find $\rho = 0.056/0.023 \approx 2.4$, in agreement with the theoretical value.

7 Parameter extraction from dark noise recordings

Experimental recordings of dark noise in wild type (WT) and GCAPs$^{-/-}$ knockout mice together can be used with expressions for the power spectrum and variance to evaluate unknown parameters invivo.

7.1 Estimation of μ_{sp} and $P^*_{sp,comp}$ from dark noise recordings in GCAPs$^{-/-}$ mice

For GCAPs$^{-/-}$ rods, the power spectrum divided by the variance (Eq. 85 and Eq. 86) reduces to a double Lorentzian that depends only on the parameters μ_{sp} and β_d:

$$\hat{S}_{\hat{I}_{os}}(\omega) = 4\frac{(\beta_d + \mu_{sp})\,\beta_d\mu_{sp}}{(\beta_d^2 + \omega^2)(\mu_{sp}^2 + \omega^2)} \tag{91}$$

Because $\beta = 4.1s^{-1}$ [26] is known for a mouse rod, we used Eq. 91 to extract the unknown spontaneous PDE deactivation rate μ_{sp}.

To extract μ_{sp}, we used the current recordings from GCAPs$^{-/-}$ mouse rods recorded in darkness and bright light conditions (Fig. 4A). The latter is needed to estimate the instrumental noise, since in bright light all channels are closed and the recorded noise is only instrumental noise [7]. Because instrumental and biological noise are independent, the dark noise power spectrum and variance can be computed by subtracting the instrumental values. Using eq. 91 to fit the dark-light power spectrum scaled by the dark-light variance, it is possible to obtain an averaged value $\mu_{sp} = 12.4s^{-1}$. Subsequently, with the values of μ_{sp} and β_d, we used Eq. 86 and fitted the unknown mean number of spontaneously activated PDE per compartment $\bar{P}^*_{sp,comp}$ using the measured dark-light variance (with $N_{comp} = 810$). We obtained an average value $\bar{P}^*_{sp,comp} = 0.9$.

7.2 Estimation of the parameters r_α and B_{ca} from dark noise recordings in WT mice

The single-photon response and the dark noise amplitude strongly depend on the calcium feedback. Eq. 90 shows that the dark noise amplitude can be reduced by a factor 4.4 due to calcium feedback. By analyzing experimental data from WT and GCAPs$^{-/-}$ mice, we found a factor around 2.4 (Fig 4 and Fig 5). The strength of the calcium feedback depends on r_α and B_{ca} (feedback on cGMP synthesis and buffering capacity). Unfortunately, both values are not precisely known. Most models assume $r_\alpha = 0$ [43, 44, 36], in [45] a value $r_\alpha = 0.072$ is used. In [36, 43] a buffering capacity $B_{ca} = 50$ is assumed, $B_{ca} = 20$ is used in [45] and $B_{ca} = 100$ in [44].

To estimate r_α and B_{ca}, we computed the dark-light power spectrum from dark noise recordings in WT rods (Fig. 5A). We fitted r_α and γ_d using Eq. 82 and then used Eq. 74 to compute B_{ca} from γ_d. By fitting the spectrum we obtained $r_\alpha = 0.066$ and $\gamma_d = 23.4s^{-1}$. With the experimental mean dark current of $17.9pA$, we then computed $B_{ca} = 80$, which is in agreement with experimental recordings [34, 46].

We used these values to simulate the dark noise in a WT rod (Fig. 4B). We quantified the agreement between data and simulations by comparing the probability distributions of the recorded and simulated current amplitudes (Fig. 4C), and by comparing the experimental dark-light spectrum with the spectrum extracted from the simulations and with the analytical expression in Eq. 82 (Fig. 5D). Although we find very good agreement for the power spectra (Fig. 5D), the standard deviation of the simulated current amplitude ($\Sigma_{sim} = 2.3\%$) is about 15% smaller than the experimental value ($\Sigma_{dark} = 2.7\%$). This difference may result from instrumental noise that increases the recorded noise

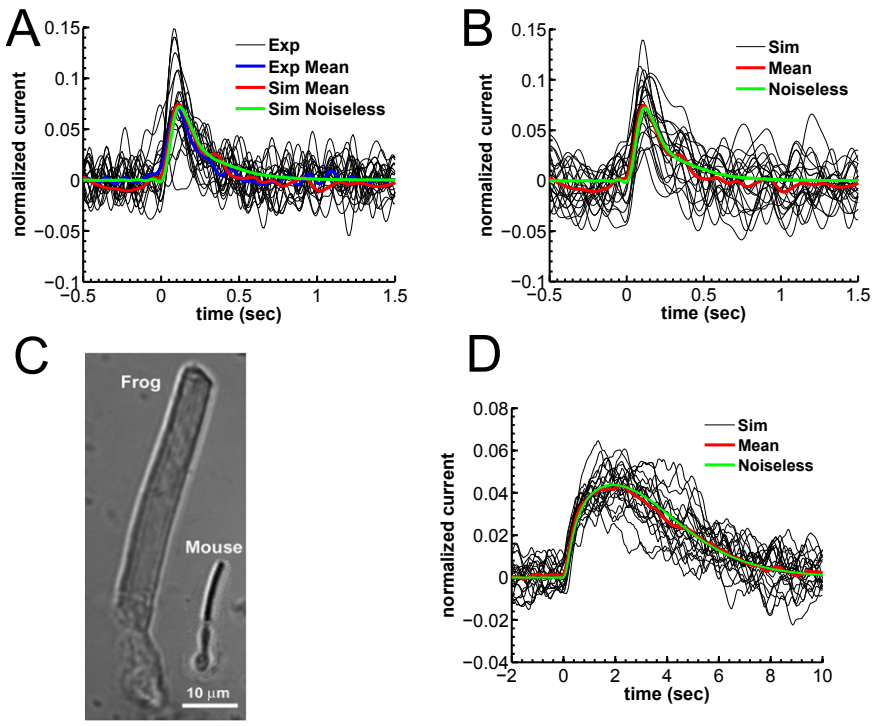

Fig. 4: **Single photon responses of mouse and toad rods.** (A) Electrophysiological recordings of single-photon responses (black) from a mouse rod together with the mean response (blue). Mean (red) and the deterministic simulation (green) from B are superimposed for comparison. Currents have been normalized to the circulating current in darkness. (B) Single-photon response simulations for a mouse rod(black) with mean (red) and a simulation of the mean response from a deterministic model without noise (green). (C) Rods from frog (toad) and mouse showing the large size difference [38]. (D) Single-photon response simulations for a toad rod ($\beta_d = 1s^{-1}$). Note the much larger duration compared to B.

Table 4: Parameter values used to simulate the photocurrent

Parameter	**Toad**	**Mouse**
N_{comp}	2000	810
R (μm)	3	0.7
h (nm)	15	15
w (nm)	15	15
a (nm)	3	3
$k_{enc}(\mathrm{s}^{-1})$	2.9	61
$k_{li}(\mathrm{s}^{-1})$	2.9	61
β_d (s^{-1})	1	4.1
g_d (μM)	3	3
c_d (μM)	0.3	0.3
$I_{os,d}$ (pA)	40	17.9
f_{ca}	0.12	0.12
γ_d (s^{-1})	92	23.4
B_{ca}	1	80
K_α (μM)	0.15	0.1
K_{ch} (μM)	20	20
K_{ex} (μM)	1.6	1.6
n_α	2	2
r_α	0	0.066
n_{ch}	3	3
D_g $(\mu m^2 s^{-1})$	150	150
$D_{g,l}$ $(\mu m^2 s^{-1})$	20	40
$D_{ca,l}$ $(\mu m^2 s^{-1})$	20	20

in darkness, which is not accounted for in the simulation. This effect is much larger for WT than GCAPs$^{-/-}$ rods because WT rods have less intrinsic dark noise.

Fig. 5: **Dark noise recordings and simulations for a GCAPs/ mouse rod.** (A) Electrophysiological current recordings in complete darkness (black) and in bright light (red). Bright light recordings are used to extract the instrumental noise. (B) Simulations of the current fluctuations in darkness (dark noise). (C) Probability distribution of the amplitudes from panels (A) and (B) together with Gaussian fits. (D) Comparison of the darklight power spectrum from A with the power spectrum from B and analytic result.

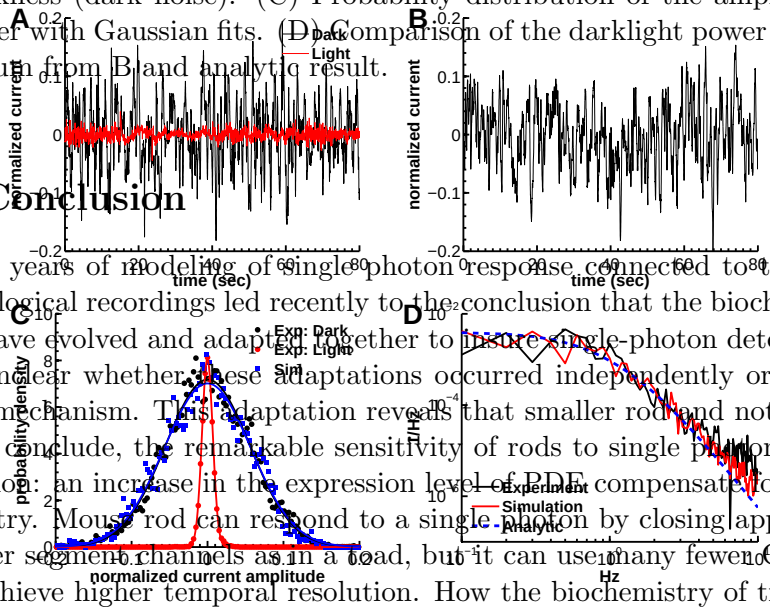

8 Conclusion

Thirty years of modeling of single photon response connected to the statistical analysis of electrophysiological recordings led recently to the conclusion that the biochemistry and geometry of the rod may have evolved and adapted together to insure single-photon detection across species [18, 38], but it is unclear whether these adaptations occurred independently or were coupled together by some other mechanism. This adaptation reveals that smaller rod and not a scaling copy larger one.

To conclude, the remarkable sensitivity of rods to single photons reveals a selection principle of evolution: an increase in the expression level of PDE compensate for the reduction in outer segment geometry. Mouse rod can respond to a single photon by closing approximately the same percentage of outer segment channels as in a toad, but it can use many fewer G proteins and effector molecules and achieve higher temporal resolution. How the biochemistry of transduction and the geometry of the outer segment may have evolved together to ensure the detection of single photons is certainly a new question to address. The surprise of these research is that the conclusion about the co-evolution of the cel geometry and the biochemistry came from the development of stochastic modeling of the underlying molecular processes. Similar modeling are expected in many other transduction processes such as heat sensing, olfaction, auditory transduction. The diversity of the cell geometries involved in transduction, that have evolved for billions of years remains an open question for modern geometry,

but the physiology needs to be taken in account.

References

[1] K.-W. Yau and R. Hardie, "Phototransduction motifs and variations.," *Cell*, vol. 139, pp. 246 – 264, 2009.

[2] Z. Song, M. Postma, S. Billings, D. Coca, R. Hardie, and M. Juusola, "Stochastic, adaptive sampling of information by microvilli in fly photoreceptors.," *Curr. Biol.*, vol. 22, no. 15, pp. 1371–1380, 2012.

[3] G. Fain, *Sensory Transduction*. Sunderland, MA: Sinauer, Inc., 2003.

[4] V. Arshavsky and M. Burns, "Photoreceptor signaling: supporting vision across a wide range of light intensities.," *J Biol Chem*, vol. 287, pp. 1620–1626, 2012.

[5] D. Baylor, T. Lamb, and K.-W. Yau, "Responses of retinal rods to single-photons.," *J. Physiol.*, vol. 288, pp. 613–634, 1979.

[6] G. Field and F. Rieke, "Mechanisms regulating variability of the single-photon responses of mammalian rod photoreceptors," *Neuron*, vol. 35, pp. 733–747, 2002.

[7] F. Rieke and D. Baylor, "Molecular origin of continous dark noise in rod photoreceptors," *Biophys. J.*, vol. 71, pp. 2553–2572, 1996.

[8] S. Nikonov, T. Lamb, and E. Pugh Jr, "The role of steady phosphodiesterase activity in the kinetics and sensitivity of the light-adapted salamander rod photoresponse," *J. Gen. Physiol.*, vol. 116, pp. 795–824, 2000.

[9] D. A. Baylor, G. Matthews, and K.-W. Yau, "Two components of electrical dark noise in toad retinal rod outer segments.," *J. Physiol.*, vol. 309, pp. 591–621, 1980.

[10] F. Rieke and D. Baylor, "Single-photon detection by rod cells of the retina," *Rev. of Mod. Phys.*, vol. 70, no. 3, pp. 1027–1036, 1998.

[11] G. Whitlock and T. Lamb, "Variablity in the time ourse of single photon responses from toad rods: termination of rhodopsin's activity," *Neuron*, vol. 23, pp. 337–351, 1999.

[12] D. Holcman and J. Korenbrot, "The limit of photoreceptor sensitivity: Molecular mechanism of dark noise in retinal cones," *J. Gen. Physiol.*, vol. 125, pp. 641–660, 2005.

[13] T. Doan, A. Mendez, P. Detwiler, J. Chen, and F. Rieke, "Multiple phosphorylation sites confer reproducibility of the rod's single-photon responses.," *Science*, vol. 13, pp. 530–3, 2006.

[14] J. Reingruber and D. Holcman, "The narrow escape problem in a flat cylindrical microdomain with application to diffusion in the synaptic cleft.," *SIAM Multiscale Modeling Simulation*, vol. 9, pp. 793–816, 2011.

[15] J. Reingruber and D. Holcman, "The dynamics of phophodiesterase activation in rods and cones," *Biophys J*, vol. 94, no. 6, pp. 1954–70, 2008.

[16] R. Hamer, S. Nicholas, D. Tranchina, P. Liebman, and T. Lamb, "Multiple steps of phosphorylation of activated rhodopsin can account for the reproducibility of vertebrate rod single-photon responses," *J. Gen. Physiol.*, vol. 122, pp. 419–444, 2003.

[17] D. T. Gillespie, "General method for numerically simulating stochastic time evolution of coupled chemical-reactions.," *J. Comp. Phys.*, vol. 22, pp. 403–434, 1976.

[18] J. Reingruber, G. Fain, and D. Holcman, "How rods respond to single photons: Key adaptations of a g-protein cascade that enable vision at the physical limit of perception.," *Bioessays*, vol. 37, no. 11, pp. 1243–52, 2015.

[19] J. Reingruber and D. Holcman, "Estimating the rate of cgmp hydrolysis by phosphodiesterase in photoreceptors.," *J Chem Phys*, vol. 129, p. 145192, 2008.

[20] D. Holcman and J. Korenbrot, "Longitudinal diffusion in retinal rod and cone outer segment cytoplasm: The consequence of the cell structure," *Biophys. J.*, vol. 86, pp. 2566–2582, 2004.

[21] D. Holcman and Z. Schuss, "The narrow escape problem.," *SIAM Review*, vol. 56, no. 2, p. 213257, 2014.

[22] D. Holcman and Z. Schuss, *Stochastic narrow escape in molecular and cellular biology: analysis and applications*. Springer, 2015.

[23] S. McLAUGHLIN and J. Brown, "Diffusion of calcium ions in retinal rods. a theoretical calculation.," *The Journal of general physiology*, vol. 77, no. 4, pp. 475–487, 1981.

[24] D. Andreucci, P. Bisegna, G. Caruso, H. Hamm, and E. DiBenedetto, "Mathematical model of spatio-temporal dynmamics of second messengers in visual transduction," *Biophys. J.*, vol. 85, pp. 1358–76, 2003.

[25] J. Reingruber and D. Holcman, "Diffusion in narrow domains and application to phototransduction.," *Phys Rev E*, vol. 79, no. 3, p. 030904, 2009.

[26] O. Gross, E. N. Pugh, and M. Burns, "Spatiotemporal cgmp dynamics in living mouse rods.," *Biophys. J.*, vol. 102, no. 8, pp. 1775–1784, 2012.

[27] I. Leskov, V. Klenchin, J. Handy, G. Whitlock, V. Govardovskii, M. Bownds, T. Lamb, E. Pugh Jr, and V. Arshavsky, "The gain of rod phototransdcuction:reconciliation of biochemical and electrophysiological measurements," *Neuron*, vol. 27, pp. 525–537, 2000.

[28] Y. Koutalos, K. Nakatani, and K.-W. Yau, "Cyclic gmp diffusion coefficient in rod photoreceptors outer segment," *Biophys. J.*, vol. 68, pp. 373–382, 1995.

[29] A. Singer, Z. Schuss, D. Holcman, and B. Eisenberg, "Narrow escape i," *J. Stat. Phys.*, vol. 122, no. 3, pp. 437–536, 2006.

[30] Z. Schuss, *Theory and Applications of Stochastic Differential Equations*. Wiley Series in Probability and Statistics, John Wiley Sons, Inc., New York, 1980.

[31] H. Carslaw and J. Jaeger, *Conduction of Heat in Solids*. Oxford University Press, USA, 2 edition ed., 1986.

[32] M. E. Burns, A. Mendez, J. Chen, and D. A. Baylor, "Dynamics of cyclic gmp synthesis in retinal rods.," *Neuron.*, vol. 36, p. 8191, 2002.

[33] C. Makino, X. Wen, E. Olshevskaya, I. Peshenko, A. Savchenko, and A. Dizhoor, "Enzymatic relay mechanism stimulates cyclic gmp synthesis in rod photoresponse: biochemical and physiological study in guanylyl cyclase activating protein 1 knockout mice.," *PLoS One*, vol. 7, no. 10, p. e47637, 2012.

[34] A. Dizhoor, E. Olshevskaya, and I. Peshenko, "Mg2+/ca2+ cation binding cycle of guanylyl cyclase activating proteins (gcaps): role in regulation of photoreceptor guanylyl cyclase.," *Mol Cell Biochem.*, vol. 334, pp. 117–124, 2010.

[35] A. Mendez, M. Burns, I. Sokal, A. Dizhoor, W. Baehr, K. Palczewski, D. Baylor, and J. Chen, "Role of guanylate cyclase-activating proteins (gcaps) in setting the flash sensitivity of rod photoreceptors.," *Proc Natl Acad Sci U S A*, vol. 98, pp. 9948–9953, 2001.

[36] E. Pugh Jr and T. Lamb, "Phototransduction in vertebrate rods and cones: Molecular mechanism of amplification, recovery and light adaptation," *In Handbook of Biological Physics Vol. 3, Elsevier Science B. V., Amsterdam*, pp. 183–255, 2000.

[37] L. Cervetto, L. Lagnado, R. Perry, D. Robinson, and P. McNaughton, "Extrusion of calcium from rod outer segments is driven by both sodium and potassium gradients.," *Nature*, vol. 337, pp. 740–743, 1989.

[38] J. Reingruber, J. Pahlberg, M. Woodruff, A. Sampath, G. Fain, and D. Holcman, "Detection of single photons by rod photoreceptors," *Proc Natl Acad Sci U S A*, vol. 110, no. 48, pp. 19378–83, 2013.

[39] C. Chen, M. Woodruff, F. Chen, D. Chen, and G. Fain, "Background light produces a recoverin-dependent modulation of activated-rhodopsin lifetime in mouse rods.," *J Neurosci*, vol. 30, pp. 1213–1220, 2010.

[40] M. Woodruff, K. Janisch, I. Peshenko, A. Dizhoor, S. Tsang, and G. Fain, "Modulation of phosphodiesterase6 turnoff during background illumination in mouse rod photoreceptors.," *J Neurosci*, vol. 28, pp. 2064–2074, 2008.

[41] M. Burns and E. Pugh Jr, "Rgs9 concentration matters in rod phototransduction.," *Biophys. J.*, vol. 16, pp. 1538–47, 2009.

[42] M. Heck and K. Hofmann, "Maximal rate and nucleotide dependence of rhodopsin-catalyzed transducin activation: initial rate analysis based on a double displacement mechanism.," *J Biol Chem*, vol. 276, pp. 10000–10009, 2001.

[43] O. Gross, E. N. Pugh, and M. Burns, "Calcium feedback to cgmp synthesis strongly attenuates single-photon responses driven by long rhodopsin lifetimes.," *Neuron*, vol. 76, no. 2, pp. 370–82, 2012.

[44] R. Hamer, S. Nicholas, D. Tranchina, T. Lamb, and J. Jarvinen, "Toward a unified model of vertebrate rod phototransduction," *Vis. Neurosci.*, vol. 22, pp. 417–436, 2005.

[45] G. Caruso, P. Bisegna, D. Andreucci, L. Lenoci, V. Gurevich, H. Hamm, and E. DiBenedetto, "Identification of key factors that reduce the variability of the single photon response.," *Proc Natl Acad Sci U S A*, vol. 108, pp. 7804–7, 2011.

[46] I. Peshenko and A. Dizhoor, "Ca2+ and mg2+ binding properties of gcap-1. evidence that mg2+-bound form is the physiological activator of photoreceptor guanylyl cyclase.," *J Biol Chem.*, vol. 281, no. 33, pp. 23830–41, 2006.